Enabling multi-material gradient structure in laser powder bed fusion

Demir A.G., Kim J., Caltanissetta F., Hart A.J., Tasan C.C., Previtali B., Colosimo B.M.

Towards multi-material additive manufacturing via laser powder bed fusion: A case study of Mn-graded steel

Ali Gökhan Demir[1*], Jinwoo Kim[2], Fabio Caltanissetta[1], A. John Hart[3],

C. Cem Tasan[2], Barbara Previtali[1], Bianca Maria Colosimo[1]

[1] Department of Mechanical Engineering, Politecnico di Milano, Via La Masa 1, 20156 Milan, Italy

[2] Department of Materials Science and Engineering, Massachusetts Institute of Technology, 77 Massachusetts Avenue, Cambridge, MA 02139, United States

[3] Department of Mechanical Engineering, Massachusetts Institute of Technology, 77 Massachusetts Avenue, Cambridge, MA 02139, United States

*Corresponding author: aligokhan.demir@polimi.it

Towards multi-material additive manufacturing via laser powder bed fusion: A case study of Mn-graded steel

Ali Gökhan Demir[1*], Jinwoo Kim[2], Fabio Caltanissetta[1], A. John Hart[3], C. Cem Tasan[2], Barbara Previtali[1], Bianca Maria Colosimo[1]

[1] Department of Mechanical Engineering, Politecnico di Milano, Via La Masa 1, 20156 Milan, Italy

[2] Department of Materials Science and Engineering, Massachusetts Institute of Technology, 77 Massachusetts Avenue, Cambridge, MA 02139, United States

[3] Department of Mechanical Engineering, Massachusetts Institute of Technology, 77 Massachusetts Avenue, Cambridge, MA 02139, United States

*Corresponding author: aligokhan.demir@polimi.it

Abstract

The layer-by-layer building in the laser powder bed fusion (LPBF) process can be exploited to achieve graded alloy compositions along the build direction. The local control over alloying element composition would allow for tailored material properties. This work demonstrates the use of LPBF to achieve gradient structures by mixing two austenitic steels, namely AISI 316L and Fe35Mn, by varying the relative deposition amounts of two alloy feedstocks. For this, a custom-built LPBF system equipped with a double-hopper and a mixing chamber was used. The system allowed the powders to be mixed on demand before deposition of each layer. The process parameters were studied to produce graded specimens starting from AISI 316L, and gradually changing to Fe35Mn, along the build direction. Characterization of the elemental composition verified good mixing of the elements, both due to the preparation of the mixed powder within the machine, and homogeneous melting of each new layer into the underlying layer of the build. Element-wise chemical composition control was therefore achieved by gradually substituting Ni, Cr, and Mo (in AISI 316L) with Mn (in Fe35Mn). The specimens were characterized for their mechanical properties at different chemical compositions along the build direction. The microhardness and the ultimate tensile strength could be varied from 240 HV to 150 HV and from 750 MPa to 600 MPa over 6 mm distance along the build direction. The results confirmed the functional gradient and the possibility to use this technique to design complex components with locally specified mechanical properties and geometry.

1. Introduction

Laser powder bed fusion (LPBF) is arguably the most widely employed additive manufacturing process at an industrial scale for producing metallic components. The geometrical freedom provided by the process allows to enhance the component performance by lightweight design, the use of lattice structures, and internal features, and the capacity to integrate several parts into a single one, which are not available to conventional manufacturing processes. On the other hand, a key limit to LPBF is the scarcity of the alloy types available for the process. Such limitation is related to the fast heating and cooling cycles induced by the laser beam within the process, which requires materials that are typically characterized by good weldability. The cost and complexity of powder production methods are other contributing factors. The LPBF processes currently employed are typically designed for printing of components from a single material. However, most industrial applications call for a combination of properties, difficult to be realized using a single material. The use of different metallic alloys in the same component is thus highly desirable. To this end, the layer-by-layer material build up capacity of the LPBF process can be exploited to vary the material composition where required, to achieve novel and tailored material properties within the component.

In literature several attempts have been made to process multiple metallic materials within a single additive manufacturing process (Vaezi et al., 2013). Figure 1 shows the different strategies for multi-material use in LPBF. One of the most straightforward way of employing new material composition is through the use of premixed alloys or pure element powder feedstocks. Such a strategy provides in-situ alloying or the production of composite materials (Li et al., 2017). The material composition remains constant throughout the whole component.

Recent research demonstrated the use of novel powder deposition systems on LPBF machines to achieve spatial material variations on demand. Material switch between layers has been commonly applied between alloys that show metallurgical compatibility (Exner et al., 2003; Liu et al., 2014; Mei

et al., 2019; Sing et al., 2015). For instance Liu et al. (Liu et al., 2014) showed the material switch between layers with stainless steel and C18400 copper alloy, while Mei et al. employed material switch between AISI 316L stainless and Inconel (Mei et al., 2019) as examples of metallurgical compatibility. Sing et al. (Sing et al., 2015) switched between AlSi10Mg and C18400 copper alloy studying the formed intermetallics in the interlayer. In these works, industrial LPBF systems were employed, where material is changed at the desired layer manually. The material switch within layers indeed requires novel deposition solutions, which proved the potential to achieve material switch between metallurgically compatible metals for producing complex parts. Mumtaz et al. (Mumtaz and Hopkinson, 2007) employed an open LPBF platform for grading between Waspalloy and partially stabilized zirconia. Ott and Zaeh (Ott and Zaeh, 2010) proposed a novel machine architecture for releasing different powder types on demand between layers. Astaett et al. (Anstaett et al., 2017) proposed a method based on powder layup and removal for mixing materials also within layers. The group of Li on the other hand demonstrated a hopper-nozzle system for laying the powder where required and removing the excess by local vacuum action providing means for complex parts changing material between and within layers (Wei et al., 2018).

On the other hand, the graded transition in LPBF is still an open field in research. This would require the continuous mixing of different materials along the process. Such approach has been analysed for instance in laser metal deposition (LMD), where material change can be regulated through the powder feed rates of the mixed materials (Brueckner et al., 2018). The discrete powder layup process appears to be limiting for the purpose. Essentially a mixing stage between the consecutive layers with different material blends would be more advantageous for a gradual change. According to the review of (Neirinck et al., 2021) the use of multiple powder hoppers and a mixing stage before powder layup, which has been also adapted in this work, is highly advantageous for a functionally graded interface allowing also to reducing stress gradients between dissimilar materials. Moreover, the graded transition does not depend on the mixing between consecutive layers through remelting, but it is determined by the dosed amount of powder feedstocks in the mixing chamber. This allows a more

homogenous transition despite a discrete change of material composition change between layers. Along with the machine architecture, the correct processing strategies can provide the means for a gradual transition between the layers in LPBF (Scaramuccia et al., 2020). This would indeed require the choice of the correct material compositions with metallurgical compatibility avoiding cracking and delamination. Potentially, if the material compositions are carefully selected, the chemical composition can be varied element-wise along the grading direction in terms of a single or multiple alloying elements. Such material grading at the level of chemical composition of the alloys requires constant material mixing capability in the LBPF system and has not been reported previously.

Accordingly, this work provides a systematic study starting from the material choice to the specimen production with a flexible multi-material LPBF platform to the final mechanical characterization. The results show the adequacy of the approach to vary the chemical composition to tailor the local mechanical properties of the LPBF alloys. The work deals with the graded LPBF of two austenitic steels for achieving controlled element-wise chemical composition variation along the grading direction. In particular Fe35Mn is added gradually to AISI 316L stainless steel to achieve gradual substitution of Cr, Ni, and Mo with Mn.
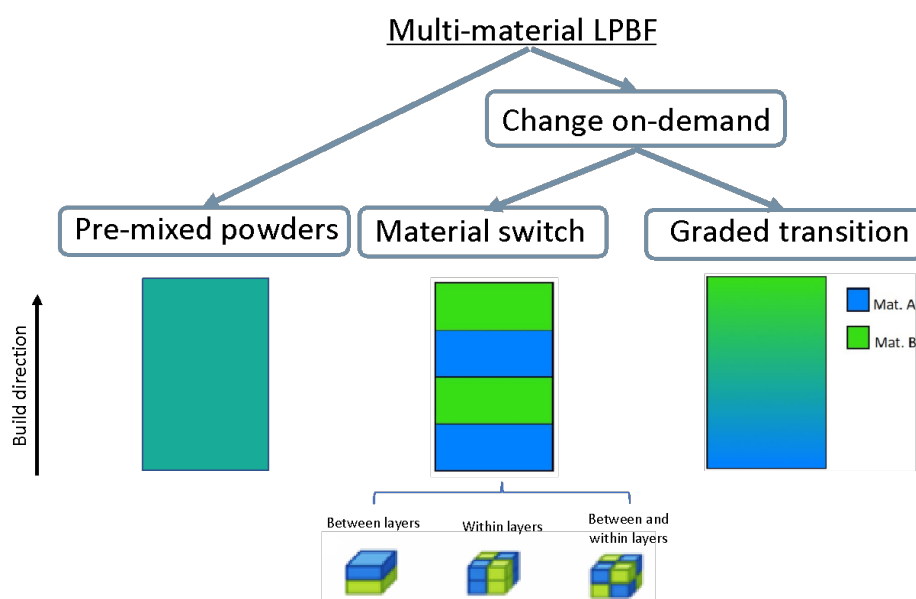

Figure 1. Different paths for multi-material use in LPBF.

2. Open LPBF platform with multi-graded processing capability

An open prototype LPBF platform named *Powderful* was used throughout this work (Demir and Previtali, 2017). The multi-material capability was provided by a double-hopper system (see Figure 2). The system design allows to change the material between layers and on demand. Hence gradient transitions can be achieved along the build direction. Two types of powders in limited quantities (<500 g) are placed in separate hoppers. The two hoppers dose the required quantity to a mixing chamber by means of piezoelectric transducers into a mixing chamber. The dosed powders are blended by means of rotating blades. The rotating blades are designed to mix or discharge the powder, depending on the rotation direction. By the end of the mixing phase the blended powder is discharged into a lower hopper, and then released on the powder bed using another piezoelectric transducer at each layer. The powder recoating system consists of an elastomer wiper. In order to dose the required powder quantity, the piezoelectric transducers are calibrated to release the required amount by controlling the vibration duration. Eventually, the unused and excess blended powder in the lower hopper is discharged before producing a new blend. The powder bed is separate from the optical chain and is enclosed in a processing chamber. Prior to processing, vacuum is applied to the process chamber down to -950 mbar and then Ar is purged up to 10 mbar. This cycle is applied three times. The laser source employed was a 1 kW single mode fiber laser (nLIGHT alta, Vancouver, WA, USA). The laser beam was collimated with a 75 mm lens and focused with a 420 mm f-theta lens encased in a scanner head (Smart Move GmbH, Garching bei München, Germany). In this configuration, the calculated beam diameter at the focal plane (d_0) is 78 μm. The scan path trajectories as well as laser process assignment were carried out with SCANMASTER software (Cambridge Technologies, Bedford, MA). The system automation was carried out in LabVIEW environment (National Instruments, Austin, TX). The main system characteristics are shown in Table 1.

Table 1 Main characteristics of the open LPBF platform _Powderful_.

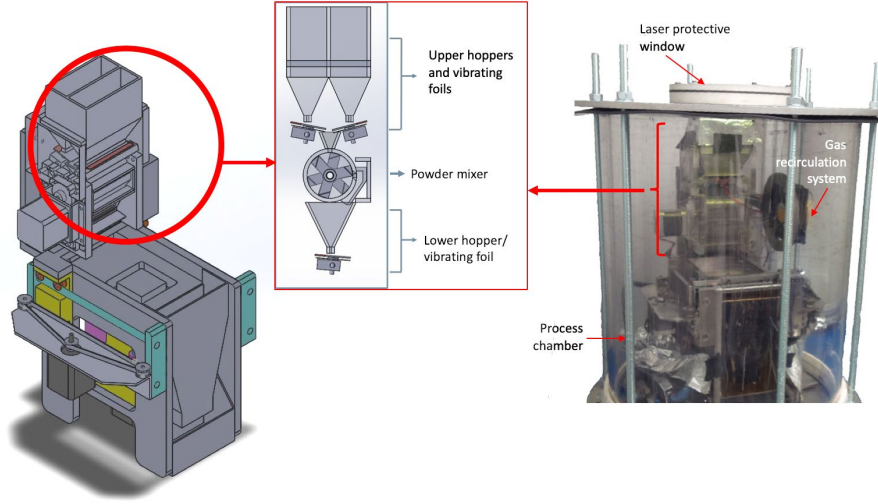| Parameter	Value
Laser emission wavelength, λ	1070 nm
Max. laser power, P_{max}	1000 W
Beam quality factor, M^2	1.19
Nominal beam diameter on focal plane, d_0	78 µm
Build platform area (DxWxH)	60x60x20 mm^3

Figure 2. _Powderful_, the in-house developed LPBF system with multi-material capability.

3. Material choice

To create graded transition of a single element across different layers is a challenging task, requiring careful consideration of the starting materials. The use of pure elements for achieving graded alloys generates safety complications, since powders of the pure elements can be highly toxic. On the other hand, when different alloy powders are mixed, stark differences in terms of solidification temperatures, distance between solidus and liquidus temperatures, and thermal conductivities can generate process instabilities leading to pores and cracks (Martin et al., 2017). As a first proof of principle investigation, we explore a compositional gradient of the Mn in an austenitic stainless steel, AISI 316L. Mn is an austenite stabilizer and changes in its content can significantly alter the mechanical response of the material, for example, from exhibiting dislocation-mediated plasticity to transformation-induced plasticity (TRIP), to twinning-induced plasticity (TWIP) (De Cooman et al., 2018). However, Mn is also a challenging alloying element to control due to its ease of evaporation

7

loss during traditional casting processes (Gasik, 2013). The use of high Mn alloys for novel steel types by LPBF has been recently investigated. The use of high Mn content and in-situ alloying for producing novel steels has been shown by Ewald et al., 2019. The TWIP behaviour could be achieved using the tailored high alloyed Mn-steel processed by LPBF (Motaman et al., 2020). Using LPBF, Köhnen et al., 2020 showed that the mechanical properties of high Mn alloys can be manufactured by controlling the laser energy and the fraction of Al blended to a premixed powder. Here in this first investigation, we alter the Mn content only in a compositional range where the dislocation-mediated plasticity is still the governing plasticity mechanism. What is expected from this change is that each layer should have slightly different yield strengths but relatively similar straining hardening rates. We chose AISI 316L and Fe35Mn as the two materials raw powders for the graded deposition. AISI 316L is an austenitic stainless steel widely used in different application such as aerospace, automotive, biomedical, and food processing. It is also one of the most widely used materials with LPBF due to its high processability. AISI 316L is characterized by good weldability, high corrosion resistance, moderate heat conductivity, and good optical absorptivity, which render the material suitable for LPBF (Casati et al., 2016). Fe35Mn is an austenitic binary alloy, which has been mainly proposed for its use in biodegradable alloy manufacturing. FeMn alloys are largely used in the steel-making industry to increase the Mn content in steels because of their lower melting point compared to the manganese oxides, thus guaranteeing an easier control of Mn addition. FeMn alloys have also important deoxidation capability and their presence stabilizes the austenitic phase of steels (decreasing the martensite start temperature).

LPBF of AISI 316L has been widely studied, since it is one of the first alloys proven to be suitable for the process (Pragana et al., 2020). The oxidation resistance of the alloy also renders it suitable for prolonged stocking in powder form. On the other hand, the processing of Fe-Mn alloys by LPBF has been more rarely studied (Carluccio et al., 2019). The recent works on the subject are mainly related to applications in biodegradable implants (D. Carluccio et al., 2020). The vaporization point of Mn is smaller than that of Fe, Ni, and Cr ($T_{v,Mn}$ =2334 K, $T_{v,Fe}$=3135 K, $T_{v,Ni}$=, 3186 K, $T_{v,Cr}$= 2944 K)

(Matweb, 2020). The large difference between the vaporization points can generate partial loss of Mn in the form of vapor during the LPBF process. The oxides on the powder can also be released during the process increasing the vapor release during the process. Hence, the processability of Fe35Mn can be expected to be lower with respect to AISI 316L.

The aimed grading is achieved by varying the Mn content starting from AISI 316L by the gradual addition of Fe35Mn. This is expected to cause substitution of the alloying elements of AISI 316L (Cr, Ni, and Mo) with Mn. Figure 3 shows the calculated fractions of the main alloying elements according to the fraction Fe35Mn added to AISI 316L starting from the nominal chemical composition of the materials. For the calculations, the mean values of Ni, Cr, and Mo in AISI 316L were used, while no material loss due to vaporization was considered. The impurities and other minor alloying elements (i.e. Si, N, S, C, P) are not shown in the plot. It is possible to observe that the calculated Fe fraction remains almost unvaried, while the Mn addition gradually substitutes Ni, Cr and Mo.
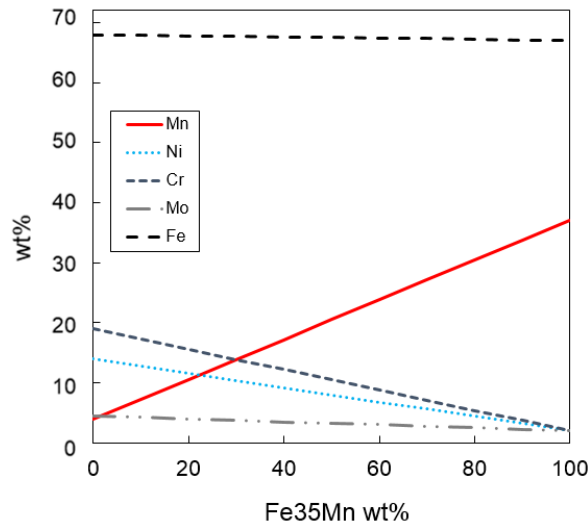

Figure 3. Calculated chemical composition variations depicting the effect of Fe35Mn addition to AISI 316L.

4. Materials and methods

4.1. Powder feedstock

The AISI 316L powder was gas atomized under Ar (Cogne Acciai Speciali S.p.a., Brescia, Italy). The particles have spherical shape and their diameters are between 15 and 45 μm. Fe35Mn powder was also gas atomized under Ar with spherical shape and particles dimensions ≤45 μm (CEAIT, San Sebastian, Spain). The powder morphology and dimension can be observed in Figure 4, whereas the nominal and measured chemical compositions are reported in Table 2.
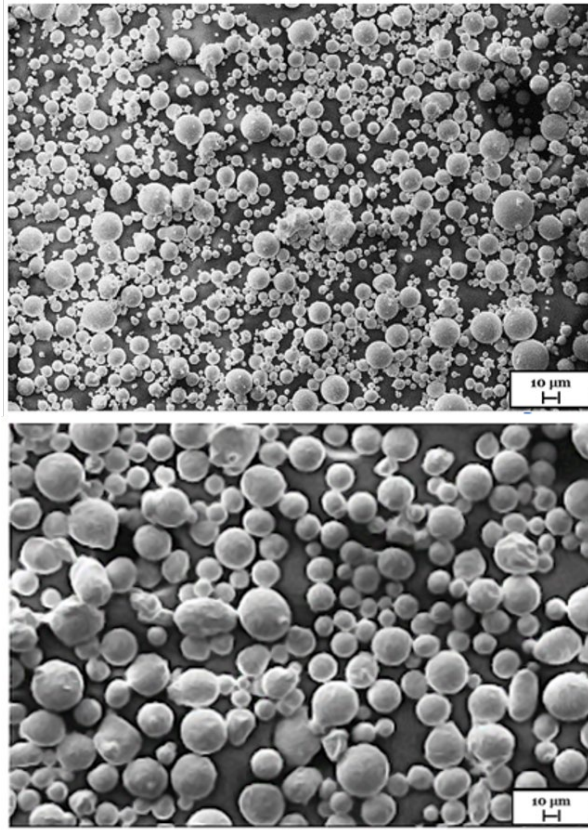

Figure 4. SEM images of the AISI 316L and Fe35Mn powders used in the experimental study.

Table 2 Chemical composition of AISI 316L and Fe35Mn powders declared by the manufacturers and measured through EDS analysis.

	wt%	C	Mn	Si	Cr	Ni	S	P	Mo	Fe
Declared	AISI 316L	0.03	0.56	0.5	16.43	11.15	0.012	0.02	2.46	Bal.
	Fe35Mn		34.4							Bal.
Measured	AISI 316L		1.8	0.61	18.56	11.2			2.35	Bal.
	Fe35Mn		35.33							Bal.

4.2. Parameter study for single alloys and pre-mixed powders

In order to select the process parameters for producing multi-graded specimens, initial tests were carried out with single alloys and pre-mixed powders. Process parameters were sought for achieving apparent density (ρ_A) values higher than 99%. In order to assess the increasing content of Mn in AISI 316L the process parameters were studied for powder mixtures containing 33 wt% and 66 wt% Fe35Mn in the AISI 316L alloy alongside with the single AISI 316L and Fe35Mn alloys. Hence the processability of materials from a complete AISI 316L concentration to Fe35Mn could be explored. Pre-mixing was carried by mixing the required quantities outside the machine. A common energy density level was sought for all the processed materials for multi-graded processing. Energy density was calculated using the following expression:

$$E = \frac{P}{vhz}$$
Eq.(1)

where P is the laser power, varied in a range of 200-500 W, scan speed varied in a range of 400-1000 mm/s, while h is the hatch distance kept fixed at 0.07 mm, z layer thickness kept at 0.05 mm with all material types apart from FeMn 66 wt%, which was processed with 0.08 mm layer thickness. The focal position (f) was kept on the powder bed plane in all tested conditions. Three cubic samples with 5x5x5 mm^3 dimensions were produced for all the tested combinations. All the process parameters are summarized in Table A. 1(Appendix A).

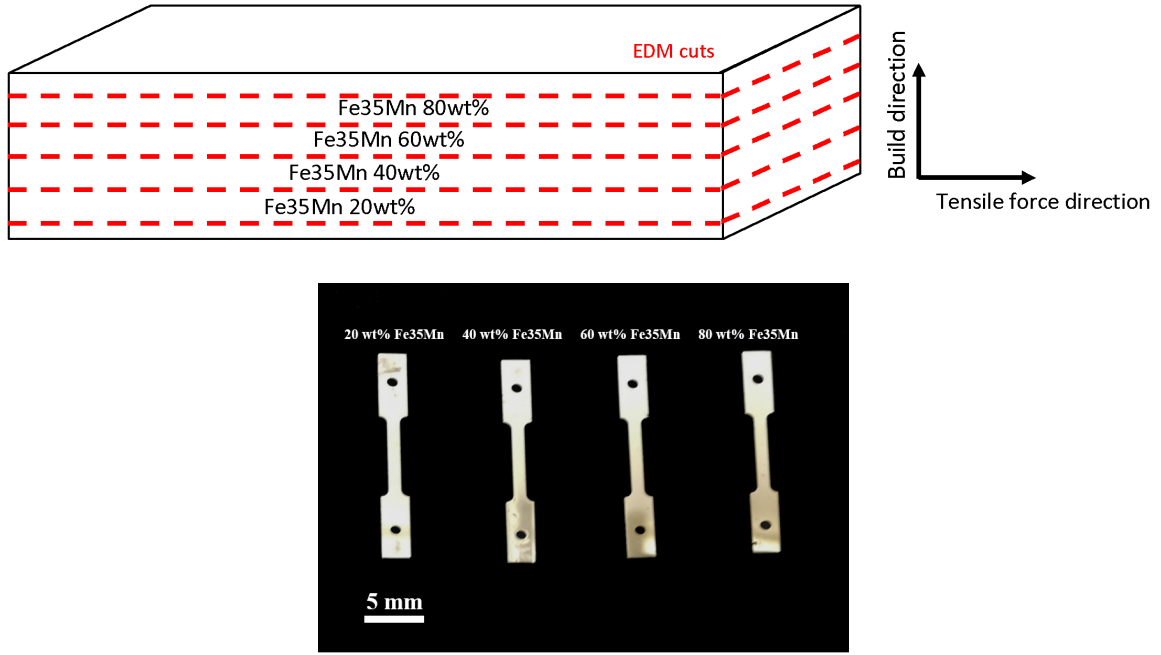|	
>10 layers	Fe35Mn
>10 layers	AISI 316L + 80 wt% Fe35Mn
>10 layers	AISI 316L + 60 wt% Fe35Mn
>10 layers	AISI 316L + 40 wt% Fe35Mn
>10 layers	AISI 316L + 20 wt% Fe35Mn
>10 layers + EXTRA for cut	AISI 316L
	SUBSTRATE

Build direction

Figure 5. (a) The designed multi-material deposition strategy. (b) The extraction of tensile samples from the built graded specimens. (c) The extracted tensile specimens.

4.3. Multi-graded processing of an AISI 316L-Fe35Mn system

Specimens with material variation along the build direction were produced starting from an AISI 316L stainless steel baseplate. The nominal specimen dimensions were 24x5.5x4.5 mm^3. Initially, 20 layers of AISI 316L were deposited in order to leave machining allowance for cutting from the base plate. The graded transition was conducted by increasing the Fe35Mn content by steps of 20 wt%. On average, 14 layers were deposited for each powder mixture reaching a total of 90 layers (see Figure 5.a). The process parameters were chosen with the results gathered from the experiments on the single alloys and the pre-mixed powders. The energy density was fixed at 204 J/mm^3 for all layers (P=350 W, v=400 mm/s, h=0.07 mm, z=0.05 mm).

4.4. Characterization

4.4.1. Density

Specimens were cut parallel to the build direction and polished employing standard metallographic preparation techniques. Optical microscopy was employed to take photographs of the entire

specimens (Mitutoyo Quick Vision ELF QV-202). Apparent density was measured from these images employing image processing software employing the following relationship.

$$\rho_A = \frac{A_{tot} - A_{pore}}{A_{tot}} \qquad\qquad \text{Eq.(2)}$$

4.4.2. Chemical composition

On graded multi-material samples, chemical composition was measured on the cross sections prepared along the building direction. EDS analysis was first performed. Line scan analysis was carried on areas of 2.4 x 2 mm. The elemental image maps obtained have a resolution 120 x 100 pixels, where each pixel is characterized by a compositional data set and corresponds to an area 0.02 x 0.02 mm of the real cross section. Images were acquired along the build direction and the element analysis was completed along the whole build height. An EBSD analysis was also performed to reveal the phases. A 400 μm wide section extended along the entire build height was analysed.

4.4.3. Mechanical properties

Vickers microhardness of the graded samples were measured along the build direction (LECO LM247AT). Indentations were performed with a load of 300 gf and an idle time of 15 seconds. Miniature tensile specimens were extracted from the graded samples at different build heights corresponding to the different chemical composition regions. Mechanical characterization was carried out with a dedicated tensile test bench for the small sample size (Gatan Microtest MTEST2000 module with 2 kN load capacity). Tensile samples were cut from graded builds by electrical discharge machining (EDM) with a kerf width of approximately 0.25 mm, where the build direction was perpendicular to the tensile axis as shown in Figure 5.b. The gauge cross-section was 2 mm (width) x 0.75 mm (thickness) x 6 mm (gauge length) as shown in Figure 5.c. Although the specimens were marked with the desired chemical composition, each sample contains some composition gradient due to this preparation phase. Tensile tests were performed at room temperature and nominal strain rate of 10^{-4} s^{-1}. The strain values of data points in stress–strain curves are recalculated by digital image correlation (DIC) using a speckle micropattern sprayed on the sample surface.

5. Results and discussion

5.1. Selection of process parameters

The processability of the single and pre-mixed alloys was characterized employing the energy density and as a function of the varied process parameters as shown in Figure 6. Although the energy density is not able to define the processability in detail, it is useful as a first order approximation (Cacace and Semeraro, 2018). Hence, it has been used in this work essentially as a means for comparison between the different material types. The overall densification behaviour followed an increasing trend over a plateau often observed in LPBF (Fayazfar et al., 2018). The differences between the single and pre-mixed alloys were observed in the processing strategies involved, which are further explained in the following.
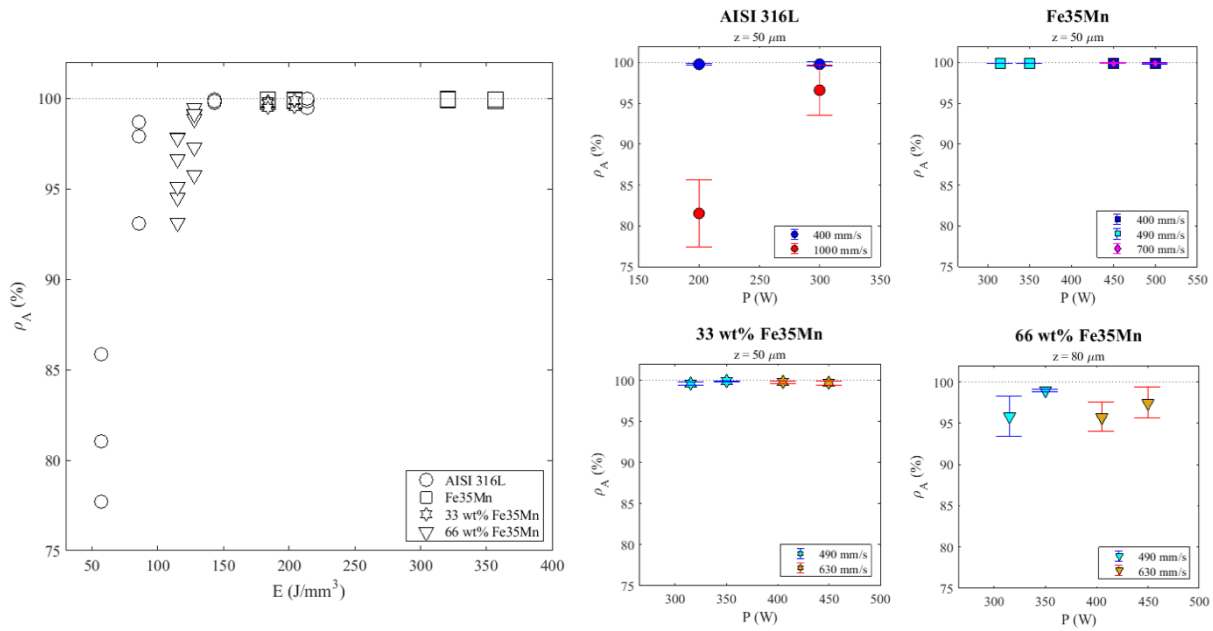
Figure 6. Apparent density of the single alloys and premixed blends as a function of energy density and as a function of laser power and scan speed. Error bars represent standard deviation

5.1.1. Processability of single alloys

Figure 7 shows three examples cross-sectioned AISI 316L specimens with different energy density below values. In terms of parameter combinations, the full densification was achieved at 400 mm/s both with 200 W and 300 W power. Lack of fusion defects dominate the porosity formation with energy density values below 143 J/mm^3, hence with higher scan speed at 1000 mm/s. Above this value, the processing conditions were found to be stable and sufficient density could be achieved.

The processing conditions for AISI 316L constituted also the energy density reference for the other tested materials.
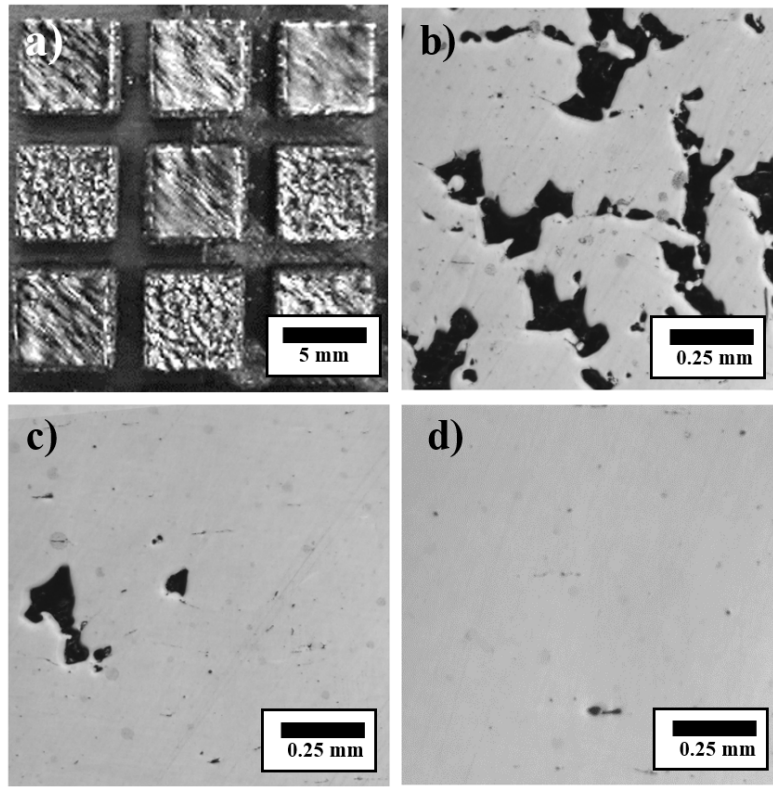

Figure 7. Top surface (a) and cross-sections of three AISI 316L specimens realized with an energy density of (b) 85.7 J/mm³, (c) 143 J/mm³, (d) 214.3 J/mm³ .

Figure 8 depicts cross-section images of the Fe35Mn specimens. With Fe53Mn the power values were between 315 W and 500 W and scan speeds between 400 mm/s and 700 mm/s. The overall combinations resulted in sufficient energy densities and adequate densification in the tested combinations. With energy density values above 147 J/mm³, apparent density values above 99.9% could be achieved. The overall processability was similar with a slightly higher of energy density required. Such difference may be related to the fact that Fe35Mn is a low alloyed material, which is prone to oxidation in powder form. Such conditions may require a higher input to release the oxide from the material (Rombouts et al., 2006).
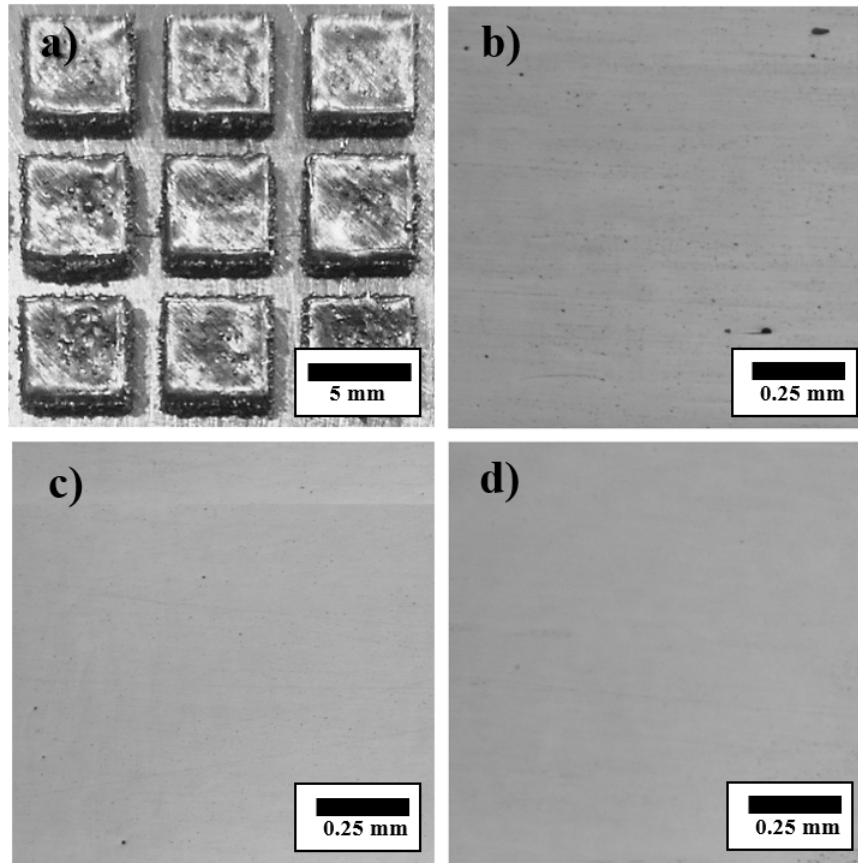
Figure 8. Top surface (a) and cross-sections of three Fe35Mn specimens realized with an energy density of (b) 184 J/mm³, (c) 204 J/mm³, (d) 321 J/mm³.

5.1.2. Processability of pre-mixed powders

In Figure 9 the cross-section images of the pre-mixed alloys produced in high apparent density conditions. For the pre-mixed powder containing 33 wt% Fe35Mn in the AISI 316L. for this pre-mixed powder combination the process parameters were investigated similar to that of the pure Fe35Mn with 315 W and 500 W and scan speeds between 490 mm/s and 630 mm/s. The investigated energy conditions ranged between 184 J/mm³ and 204 J/mm³ and fell into the plateau of processability, with apparent density values higher than 99.5 %. The processability of the pre-mixed powder with 66 wt% Fe35Mn in the AISI 316L was observed. At low energy densities part swelling and balling was observed. In order to enhance the processability the parameter combinations at high power and higher layer thickness (z=80 μm) were preferred. The laser power was varied between 315 W and 500 W and scan speeds between 490 mm/s and 630 mm/s. For this pre-mixed powder the

16

energy density parameter was not sufficient to describe the correct densification behaviour. The apparent density did not increase higher than a value of 96% at 115 J/mm^3. At 128 J/mm^3, the combination with moderate power and slower scan speed (P=350 W, v=490 mm/s) was shown to be more suitable. The reduced stability of this powder mix is attributed to the combination of balling due to the presence oxidisable Fe35Mn and in-situ alloying phenomenon occurring at the same time. The oxide release is expected to be less problematic with moderate Fe35Mn level at 33 wt%, as observed with the stability of the process in terms of densification. With higher fraction of Fe35Mn, the balling can be more localized due to heterogeneities of the powder distribution despite the mixing procedure (Li et al., 2012). Hence, the process is expected to require a more careful selection of process parameters, which is expected to determine the final melt pool size in terms of width and depth to the most suitable (Gunenthiram et al., 2018). Further analysis on melt pool dynamics through high speed imaging would be essential for a greater understanding of the phenomenon (Furumoto et al., 2018).
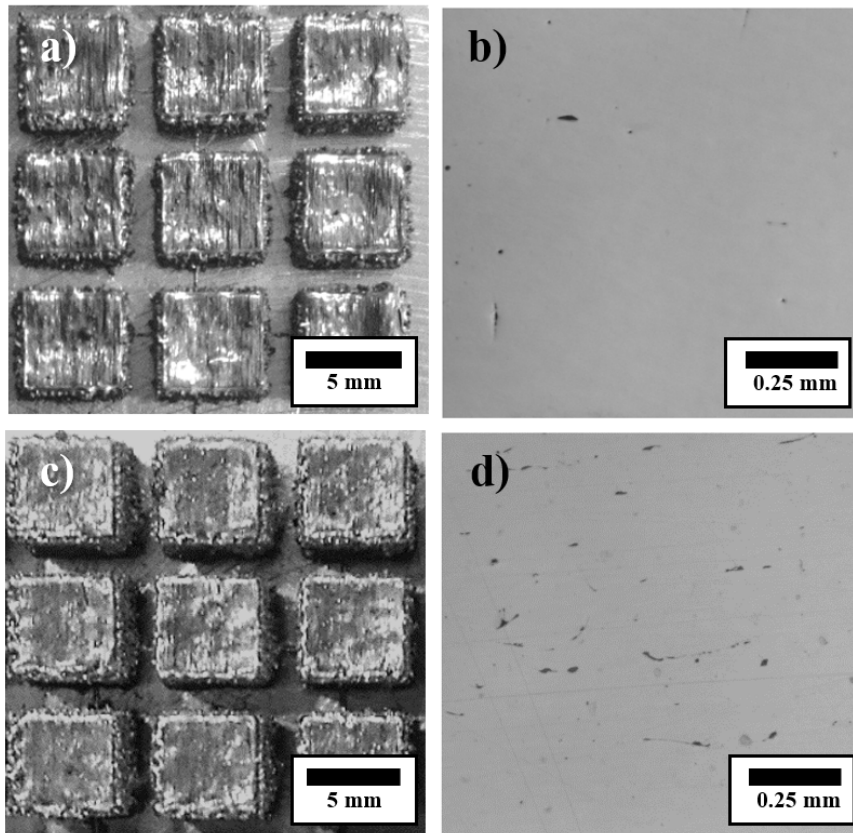

Figure 9. Top surface (a,c) and cross-sections (b,d) of pre-mixed alloys in high density conditions. (b) 33 wt% of Fe35 Mn in AISI 316L specimen realized with an energy density of 204 J/mm^3; (d) 66 wt% of Fe35 Mn in AISI 316L specimen realized with an energy density of 128 J/mm^3.

In conclusions, while all the selected energy levels brought to the production of fully dense parts for Fe35Mn and the 33% wt of Fe35 Mn in AISI 316L, AISI 316L powder showed a progressive increase of parts density, until a steady plateau respectively beyond 142 J/mm^3, as shown in Figure 7. The 66% wt of Fe35 Mn in AISI 316L had a more peculiar behaviour, since fully dense parts were obtained under the highest energy level. For all the powders in this study, an energy density higher than 204 J/mm^3 is placed beyond the plateau of processability lower limit, thus a part density higher than 99.5% is guaranteed. For this reason, this energy density level has been selected to produce the multi-graded build. Finally, the beneficial effect of laser modulation for powders containing Fe35Mn has been considered in process parameters selection for multi-graded experiments.

5.2. Graded addition of Mn in AISI 316L

The graded specimens were successfully produced with the required layer transitions. Figure 10.a depicts the specimens produced on the baseplate and Figure 10.b shows the cross-section of a graded specimen. The surface of the multigraded specimens show higher roughness and a swelling, which topography may be a sign of balling. While the specimens were overall intact, Such phenomenon may be induced by the oxygen release from the Fe35Mn powder. Moreover the custom-built LPBF system may not be sufficient in terms of keeping the build volume inert in long builds with significant oxygen release from the powder. The employed scan strategy and the emission profile proved to be effective for producing the specimens by the gradual grading. Porosity was present throughout the specimens as shown in the Figure 10.
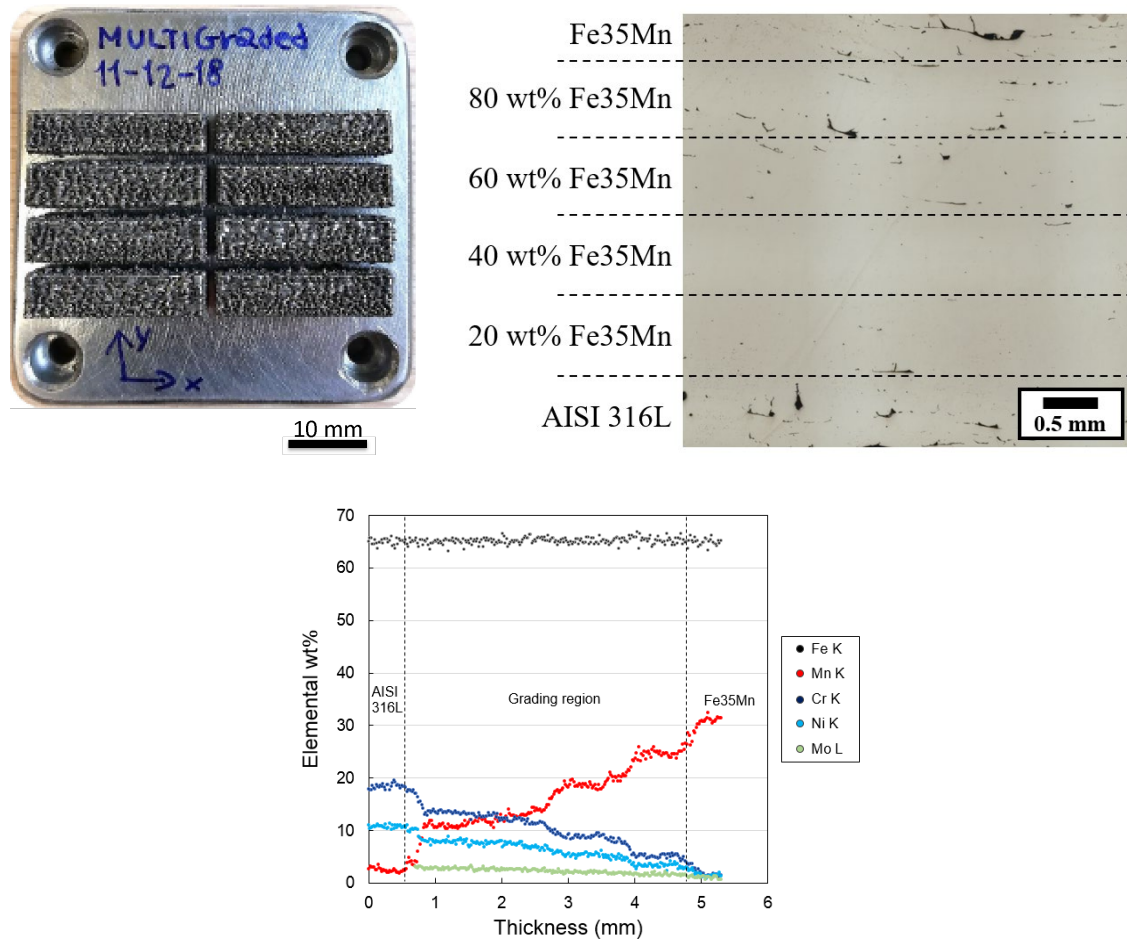
Figure 10. (a) Graded samples produced in the experimental study. (b) Cross-section image showing the porosity variation along the grading direction. (c) Chemical composition variation as function of height in the graded specimens.

5.2.1. Chemical composition and phase analysis

Figure 10.c depicts the chemical composition variation obtained along the build direction of the graded specimen. Here, in the graded region, the increase of Mn can be observed. Despite the discrete difference of the Mn contents of the layers, the gradient is monotonously increasing with slight fluctuations between the transition zones. This can be attributed to the remelting of the previous layers and the consequent mixing of the chemical compositions allowed by the thin layer thicknesses provided by LPBF. In the Fe35Mn region, a slight reduction of the Mn content with respect to the nominal composition is observed. This partial loss can be attributed to the lower vaporization point of Mn (2334 K) with respect to that of Fe (3135 K). Hence, also within the grading region the final chemical composition is expected to be affected by the losses due to vaporization. Similarly, the Cr

and Ni contents in the graded region drop from the nominal one of the AISI 316L. The Fe content over the whole build direction remains stable, confirming that the exchange is in terms of the alloying elements Mn, Cr, Ni and Mo. These observations prove that a continuous graded transition could be achieved, where effectively the Mn content was increased in the AISI 316L stainless steel to the degree where the material had no other alloying element.

Figure 11.a shows the cross-section microstructure of the graded material along the building direction (the direction from left to right in Figure 11.a-c). Pores were present at the initial part of the graded region (the right-side of Figure 11.a). The non-circular shape of the pores indicates an incomplete adhesion possibly between layers, which could be attributed to balling (Gu et al., 2013). Figure 11.b shows grain size maps obtained from EBSD scans in the areas along the building direction in Figure 11.a. The grain size was estimated from the length of the major axis of an ellipse fitting a grain. The average aspect ratio of grains (the length ratio of the minor axis to the major axis) is 0.35 ± 0.15 and the orientations of grain major axis are well aligned with the build direction as shown in Figure 11.d. This indicates that grains are elongated along the build direction, which is also the direction of the highest cooling rate. Such epitaxial growth, producing grains that elongate along several layers, has been observed on the LPBF produced austenitic AISI 316L stainless steel (Hitzler et al., 2017). Although a few large grains are observed in the high-Mn region, the grain sizes are generally distributed within a size range of 70-360 μm throughout the grading region, as presented in Figure 11.e. The EBSD phase map in Figure 11.c presents that the material is composed of austenite with a limited amount of manganese oxide less than 0.1 %. The overall observations confirm that the chemical composition variation does not affect the microstructural evolution of the material in terms of grain morphology or phases significantly.
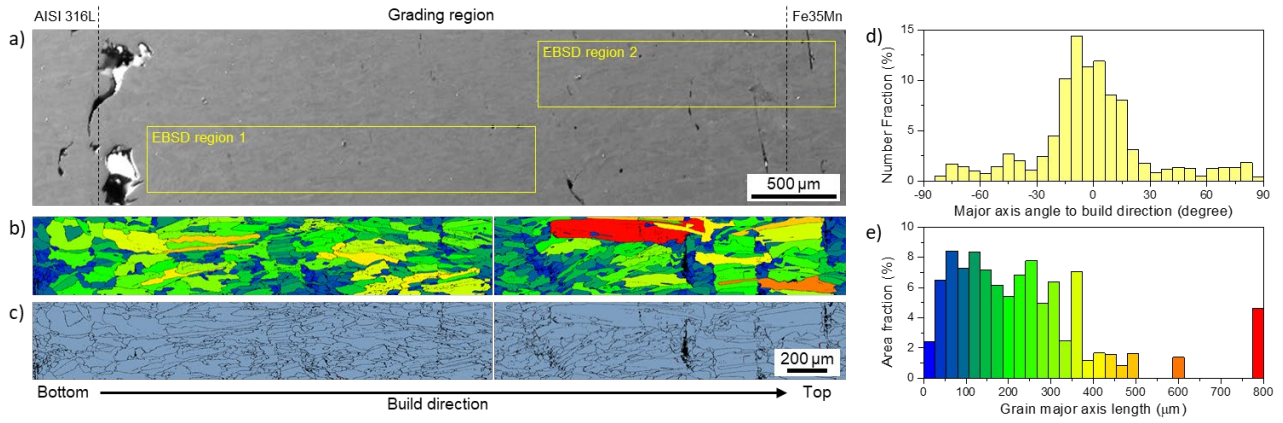
Figure 11. (a) SEM secondary electron image of the cross-section of the graded sample. (b) EBSD grain major axis size map along the build direction. The colour-size correlation is shown in e. (c) EBSD phase map (blue: austenite, black: grain boundary). The EBSD scans were performed in the areas marked with yellow boxes in a (left: region 1, right: region 2). (d) Distribution of grain major axis orientation. (e) Grain size (grain shape major axis radius) distribution obtained from the EBSD maps, plotted by area fraction. For the EBSD maps and analysis, data points with confidence index over 0.1 were used only.

5.2.2. Mechanical behaviour

As mentioned earlier, the Mn content variation in the sample is in a compositional range where the dislocation-mediated plasticity governs. In this study, we focused on the variation of hardness and strength, induced by the compositional gradient. Figure 12 shows the microhardness measurements of the graded samples along the build direction. It is observed that the hardness of AISI 316L is approximately 225 HV, which is comparable to literature (Hitzler et al., 2017). The microhardness measurements on the Fe35Mn side also showed values around 145 HV. Such value is coherent with the LPBF produced Fe35Mn in literature (Carluccio et al., 2019). In the grading region the microhardness profile appears to remain constant to the region, where the Fe35Mn was added at 60 wt%. In this region Mn content reaches over 20 wt%, while the Cr content is less than 10 wt% and the Ni content is approximately at 5 wt%.
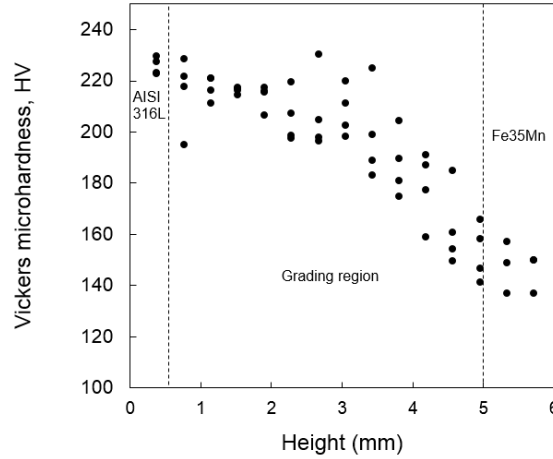
Figure 12. Vickers microhardness along the build direction of the graded specimen.

Figure 13 reports the tensile test curves corresponding the different material compositions extracted from the graded specimens along with the measured average chemical compositions. From this perspective, the graded specimens can be considered to be comprised of layers of chemical compositions not found in conventional steels. The specimens show a clear trend of decrease in the yield point as well as the ultimate tensile strength. Nevertheless, the engineering strain at fracture does not appear to follow a certain trend, which is expected to be due to an inhomogeneous distribution of pores in the layers. Indeed, previous studies have proven that a high level of porosity can generate variations in the elongation at rupture for LPBF produced materials (Casati et al., 2016). Interestingly, only the specimen of 60 wt.% Fe35Mn shows a distinct work-hardening behavior among the four specimens, which might originate from a change of plastic deformation mechanism in the composition range and needs further investigation. In Figure 14, the 0.2% yield strength (YS) and ultimate tensile strength (UTS) extracted from the tensile test curves are plotted together with the reference values of AISI 316L and Fe35Mn from literature. The graph shows a clear trend of reduction of YS and UTS as the Fe35Mn fraction in the material is increased.
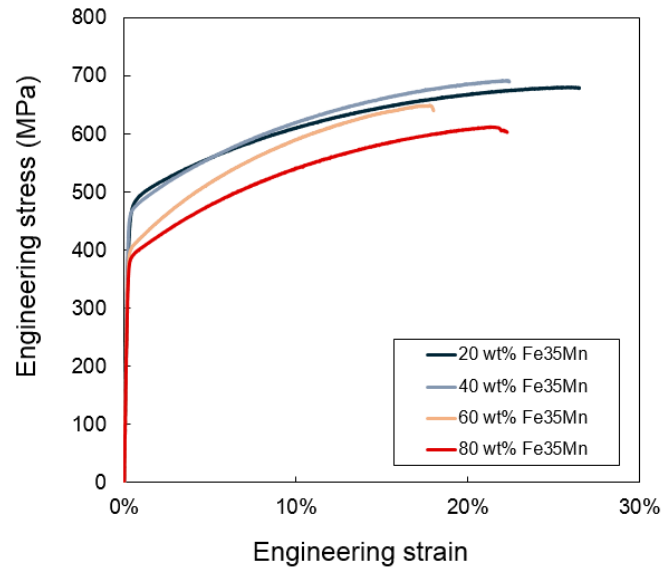
Material	Mn wt%	Cr wt%	Ni wt%	Mo wt%	Fe wt%
20 wt% Fe35Mn	11.20	13.33	7.85	2.73	Bal.
40 wt% Fe35Mn	14.15	11.36	6.89	2.43	Bal.
60 wt% Fe35Mn	21.82	6.78	4.27	1.80	Bal.
80 wt% Fe35Mn	25.40	4.57	3.03	1.65	Bal.

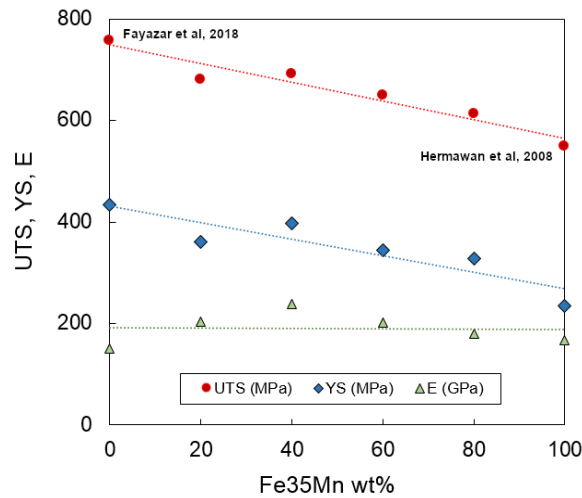**Figure 13. Tensile test curves and measured chemical compositions of the different material compositions.**

Figure 14. Ultimate tensile stress, yield stress, and elastic modulus as a function of Fe35Mn content in the AISI 316L powder. Reference data was used for AISI 316L (0 wt%) (Fayazfar et al., 2018) **and Fe35Mn (100 wt%)** (Hermawan et al., 2008)**.**

5.3 Discussion

In this work, material grading was achieved in LPBF by mixing AISI 316 and Fe35Mn, where the latter was used as a carrier of Mn as the main grading element. Although a relatively simple material combination and a single element in the exchange is considered, the process development was proven

to be very difficult. The main process defect to be tackled remained the porosity formation, while a stable processing condition throughout all the grading regions requires further attention. The results confirmed that different grading compositions require an extensive process parameter study, where the energy density parameter remain insufficient to pinpoint the processability region. The process parameter development can indeed take advantage of simulation, modelling, and in-situ monitoring means. The multiphysics simulations combining thermal field and fluid dynamics are needed to include the influence of the material mixing phenomenon, which is going to be critically important in a process development phase (Gu et al., 2020). An issue regards the complexity of non-reversible transformation between the separate powder feedstocks and the in-situ formed new alloy. The simulation capabilities should be able to adapt to this change in the material composition. While simulating the properties of materials formed through LPBF is relatively new (W. Yan et al., 2018), embedding these modelling tools within the process simulation to estimate and use the new and local material properties will require further attention. Another path for process parameter selection can be found through the in-situ monitoring. All the analyses carried out in this work relied on approaches commonly used on pre-alloyed powders based on producing specimens and analysing them. On-board analysis of the process stability through process signatures may be a solution reducing the experimental effort (Repossini et al., 2017).

As the results underline the difficulty in controlling a single element in the grading region, the machine architecture must be more precise for more complex chemical changes involving two or more elements. The relatively simple gas management system employed in the present prototype system will not suffice when materials with higher reactivity such as Ti-alloys are considered. The use of novel scan strategies, temporal and spatial beams shaping techniques can be beneficial for a greater control of heating and cooling cycles (Catchpole-Smith et al., 2017). Hence, the mixing behaviour in the melt pool, as well as the grain size and orientation can be better controlled. The use of different powder sizes and distributions can allow for a better distribution of the powder feedstocks

along the powder bed. Smaller layer thicknesses and finer steps of mixtures are expected to improve the chemical gradient along the material.

In addition, in order to further refine the steps of compositional gradient and achieve continuous gradients, one could consider post heat treatment processes combined with the printing techniques, although the applicability may depend on the composition range of gradient. The local variation of composition can result in non-uniform chemical or microstructural changes at a single temperature, and optimizing heat treatment conditions adequate for a wide range of composition in a single material would be challenging.

From a materials perspective, effects of compositional gradients on mechanical properties can be more complex, compared to other types of gradients such as grain size (Fang et al., 2011) and nano twins (Wei et al., 2014). Compositional gradients can alter the plasticity mechanisms locally (e.g. from dislocation-mediated plasticity to transformation-induced plasticity (TRIP), or twinning-induced plasticity (TWIP), opening numerous potentials in the design of novel structural materials.

On the other hand, with the achieved graded material results can be compared to the existing steel grades and allocated to possible applications. While microstructural gradients in alloys such as grain size and nanotwins have been widely studied in terms of ductility (Ke, 2014), strengthening (J. Yan et al., 2018) and work-hardening (Cheng et al., 2018) in last decades, experimental research on compositionally graded alloys has been limited due to difficulties in the material fabrication. The overall analyses in this work shows that the compositional grading in LPBF process allows to manipulate the mechanical properties of local volumes without significantly changing microstructure and phase, which provides a wide design space of graded materials with optimized mechanical properties, such as wear resistance by redistributing contact stress fields (Suresh, 2001) and multi-axial deformation resistance (Yu et al., 2017). In particular, the gradual transition of composition between layers as demonstrated in this work can improve interfacial bonding (Suresh, 2001), reduce stress concentration at interfaces (Giannakopoulos et al., 1995), and also relax thermal stresses (Koizumi and Niino, 1995). The localized differences in the yield strengths can be exploited for

controlled fracture mechanisms, such as the controlled decomposition of elements upon re-entry in atmosphere for aerospace applications. A similar approach can be employed for safe-failure devices, where material should locally yield in pressure vessels (Bourga et al., 2015). The use of graded structures would also be highly suitable along with lattice structures.

Another advantage would be the graded response of the material to corrosive environment, as previously suggested by computational works (Yu et al., 2017). The local corrosion behaviour can be controlled by means of chemical composition variation. Such strategy would be highly appealing for modulating the bio-absorption behaviour of implants. In particular, large and permanent implants can be manufactured in AISI 316L alloy with graded transition regions with Fe35Mn. AISI 316L stainless steel is widely used as a biocompatible material for orthopaedic, orthodontic, and cardiovascular applications (Sing et al., 2016). AISI 316L implants can be customized to the patient's anatomy and exploit its load bearing capability. On the other hand, LPBF produced biodegradable Fe35Mn lattices have shown to possess good osseointegration behaviour and promote bone growth during degradation (Danilo Carluccio et al., 2020). For instance, on a total hip replacement implant the attaching surfaces of the femoral stem and the acetabular cup can be produced with graded transition from Fe35Mn to AISI 316L. The use of LPBF can provide better osseointegration and bone growth while the bulk of the implant AISI 316L would remain as the load bearing permanent part.

The production of the graded materials also will require further attention from the post-processing view point. The response of the material to a given heat treatment can be different along the gradient direction. The use of local heat treatments, such as using another laser beam may be an option to adjust the microstructure locally. Indeed, the layer-by-layer build-up process within the LPBF process can provide the access to these local treatments prior to the change towards another material composition. Larger diode laser beams or vertical-cavity surface-emitting lasers (VCSEL) can be employed for such purpose (Zavala-Arredondo et al., 2018).

6. Conclusions

This work presented a systematic study of process development for producing graded metallic specimens using LPBF along with their extensive material characterization. In particular, the work showed the material selection criteria that allowed to manipulate the chemical composition of Fe-based alloys at singular element-wise level. For this purpose, AISI 316L powders were mixed with Fe35Mn and on demand employing a flexible multi-material LPBF platform producing an almost continuous Mn variation along the build direction. The main results of the work can be summarized as follows.

- The correct choice of materials for producing graded materials through LPBF requires the matching of chemical compositions as well as processability concerns. The use of two austenitic Fe-based alloys results in a successful match for producing graded components. Further studies using modelling and simulation methods including both the metallurgical and LPBF related aspects would be beneficial for ensuring the manufacturability of the graded parts.

- The processability of AISI 316L and Fe35Mn differ slightly in terms of the energy density requirements. The graded specimen production was designed through the study of the processability of the premixed powder compositions, which provided the overall production cycle.

- The graded specimens were produced by adding Fe35Mn at discrete composition levels and layer increments. Despite this fact, the remelting capacity of LPBF between the consecutive layers allowed to achieve a consistent gradient increase of Mn and decrease of Cr, Ni, and Mo, while the content of Fe remained stable as desired.

- The graded components were found to be consistent in terms of microstructure and grain size over the build direction. The mechanical properties accompanied by the chemistry variation showed significant change along the grading direction. The microhardness, yield and ultimate tensile strengths were varied significantly.

Acknowledgements

APPENDIX A

Table A. 1 Process parameters used in the experimental campaign.

	Power, P (W)	Scan speed, v (mm/s)	Hatch distance, h (mm)	Layer thickness, z (mm)	Focal position, f (mm)	Energy density, E (J/mm³)	Apparent Density - mean (%)	Apparent Density - st. dev. (%)
AISI 316L	200	400	0.07	0.05	0	143	99.8	0.10
	200	1000	0.07	0.05	0	57	81.5	4.08
	300	400	0.07	0.05	0	214	99.8	0.26
	300	1000	0.07	0.05	0	86	96.6	3.04
Fe35Mn	450	400	0.07	0.05	0	321	99.9	0.04
	450	700	0.07	0.05	0	184	99.9	0.05
	315	490	0.07	0.05	0	184	99.9	0.02
	500	400	0.07	0.05	0	357	99.9	0.06
	500	700	0.07	0.05	0	204	99.9	0.03
	350	490	0.07	0.05	0	204	99.9	0.03
Fe35Mn 33%wt	315	490	0.07	0.05	0	184	99.6	0.20
	405	630	0.07	0.05	0	184	99.8	0.15
	350	490	0.07	0.05	0	204	99.9	0.04
	450	630	0.07	0.05	0	204	99.7	0.25
Fe35Mn 66%wt	315	490	0.07	0.08	0	115	95.9	2.44
	405	630	0.07	0.08	0	115	95.8	1.77
	350	490	0.07	0.08	0	128	99.0	0.15
	450	630	0.07	0.08	0	128	97.5	1.87

References

Anstaett, C., Seidel, C., Reinhart, G., 2017. Fabrication of 3D Multi-material Parts Using Laser-based Powder Bed Fusion, in: Proceedings of the 28th Annual International Solid Freeform Fabrication Symposium–An Additive Manufacturing Conference. pp. 1–9.

Bourga, R., Moore, P., Janin, Y.J., Wang, B., Sharples, J., 2015. Leak-before-break: Global perspectives and procedures. Int. J. Press. Vessel. Pip. 129, 43–49. doi:10.1016/j.ijpvp.2015.02.004

Brueckner, F., Riede, M., Müller, M., Marquardt, F., Willner, R., Seidel, A., Lopéz, E., Leyens, C., Beyer, E., 2018. Enhanced manufacturing possibilities using multi-materials: In laser metal deposition. LIA Today 26, 10–12. doi:10.2351/1.5040639

Cacace, S., Semeraro, Q., 2018. About Fluence and Process Parameters on Maraging Steel Processed by Selective Laser Melting: Do They Convey the Same Information? Int. J. Precis. Eng. Manuf. 19, 1873–1884. doi:10.1007/s12541-018-0204-y

Carluccio, D., Demir, A.G., Bermingham, M.J., Dargusch, M.S., 2020. Challenges and Opportunities in the Selective Laser Melting of Biodegradable Metals for Load-Bearing Bone Scaffold Applications. Metall. Mater. Trans. A Phys. Metall. Mater. Sci. doi:10.1007/s11661-020-05796-z

Carluccio, D., Demir, A.G., Caprio, L., Previtali, B., Bermingham, M.J., Dargusch, M.S., 2019. The influence of laser processing parameters on the densification and surface morphology of pure Fe and Fe-35Mn scaffolds produced by selective laser melting. J. Manuf. Process. 40, 113–121. doi:10.1016/j.jmapro.2019.03.018

Carluccio, Danilo, Xu, C., Venezuela, J., Cao, Y., Kent, D., Bermingham, M., Demir, A.G., Previtali, B., Ye, Q., Dargusch, M., 2020. Additively manufactured iron-manganese for biodegradable porous load-bearing bone scaffold applications. Acta Biomater. 103, 346–360. doi:10.1016/j.actbio.2019.12.018

Casati, R., Lemke, J., Vedani, M., 2016. Microstructure and Fracture Behavior of 316L Austenitic Stainless Steel Produced by Selective Laser Melting. J. Mater. Sci. Technol. 32, 738–744. doi:10.1016/j.jmst.2016.06.016

Catchpole-Smith, S., Aboulkhair, N., Parry, L., Tuck, C., Ashcroft, I.A., Clare, A., 2017. Fractal scan strategies for selective laser melting of 'unweldable' nickel superalloys. Addit. Manuf. 15, 113–122. doi:10.1016/j.addma.2017.02.002

Cheng, Z., Zhou, H., Lu, Q., Gao, H., Lu, L., 2018. Extra strengthening and work hardening in gradient nanotwinned metals. Science (80-.). 362. doi:10.1126/science.aau1925

De Cooman, B.C., Estrin, Y., Kim, S.K., 2018. Twinning-induced plasticity (TWIP) steels. Acta Mater. 142, 283–362. doi:10.1016/j.actamat.2017.06.046

Demir, A.G., Previtali, B., 2017. Multi-material selective laser melting of Fe / Al-12Si components. Manuf. Lett. J. 11, 8–11. doi:10.1016/j.mfglet.2017.01.002

Ewald, S., Kies, F., Hermsen, S., Voshage, M., Haase, C., Schleifenbaum, J.H., 2019. Rapid alloy development of extremely high-alloyed metals using powder blends in laser powder bed fusion. Materials (Basel). 12, 1–15. doi:10.3390/MA12101706

Exner, H., Regenfuss, P., Hartwig, L., Klötzer, S., Ebert, R., 2003. Selective Laser Micro Sintering with a Novel Process 5063, 145–151.

Fang, T.H., Li, W.L., Tao, N.R., Lu, K., 2011. Revealing Extraordinary Intrinsic Tensile Plasticity in Gradient Nano-Grained Copper. Science (80-.). 331, 1587–1590.

Furumoto, T., Egashira, K., Munekage, K., Abe, S., 2018. Experimental investigation of melt pool behaviour during selective laser melting by high speed imaging. CIRP Ann. 67, 253–256. doi:10.1016/j.cirp.2018.04.097

Gasik, M. (Ed.), 2013. Handbook of Ferroalloys. Elsevier.

Giannakopoulos, A.E., Suresh, S., Finot, M., Olsson, M., 1995. Elastoplastic analysis of thermal cycling: layered materials with compositional gradients. Acta Metall. Mater. 43, 1335–1354.

doi:10.1016/0956-7151(94)00360-T

Gu, H., Gong, H., Pal, D., Rafi, K., Starr, T., Stucker., B., 2013. Influences of Energy Density on Porosity and Microstructure of Selective Laser Melted 17- 4PH Stainless Steel, in: 2013 Solid Freeform Fabrication Symposium (Vol. 474). pp. 474–489.

Gu, H., Wei, C., Li, L., Han, Q., Setchi, R., Ryan, M., Li, Q., 2020. Multi-physics modelling of molten pool development and track formation in multi-track, multi-layer and multi-material selective laser melting. Int. J. Heat Mass Transf. 151, 119458. doi:10.1016/j.ijheatmasstransfer.2020.119458

Gunenthiram, V., Peyre, P., Schneider, M., Dal, M., Coste, F., Koutiri, I., Fabbro, R., 2018. Experimental analysis of spatter generation and melt-pool behavior during the powder bed laser beam melting process. J. Mater. Process. Technol. 251, 376–386. doi:10.1016/j.jmatprotec.2017.08.012

Hitzler, L., Hirsch, J., Heine, B., Merkel, M., Hall, W., Öchsner, A., 2017. On the anisotropic mechanical properties of selective laser-melted stainless steel. Materials (Basel). 10. doi:10.3390/ma10101136

Ke, L., 2014. Making strong nanomaterials ductile with gradients. Science (80-.). 345, 1455 LP – 1456.

Köhnen, P., Ewald, S., Schleifenbaum, J.H., Belyakov, A., Haase, C., 2020. Controlling microstructure and mechanical properties of additively manufactured high-strength steels by tailored solidification. Addit. Manuf. 35, 101389. doi:10.1016/j.addma.2020.101389

Koizumi, M., Niino, M., 1995. Overview of FGM Research in Japan. MRS Bull. 20, 19–21. doi:10.1557/S0883769400048867

Li, R., Liu, J., Shi, Y., Wang, L., Jiang, W., 2012. Balling behavior of stainless steel and nickel powder during selective laser melting process. Int. J. Adv. Manuf. Technol. 59, 1025–1035. doi:10.1007/s00170-011-3566-1

Li, X.P., Ji, G., Chen, Z., Addad, A., Wu, Y., Wang, H.W., Vleugels, J., Van Humbeeck, J., Kruth, J.P., 2017. Selective laser melting of nano-TiB2decorated AlSi10Mg alloy with high fracture strength and ductility. Acta Mater. 129, 183–193. doi:10.1016/j.actamat.2017.02.062

Liu, Z.H., Zhang, D.Q., Sing, S.L., Chua, C.K., Loh, L.E., 2014. Interfacial characterization of SLM parts in multi-material processing: Metallurgical diffusion between 316L stainless steel and C18400 copper alloy. Mater. Charact. 94, 116–125.

Martin, J.H., Yahata, B.D., Hundley, J.M., Mayer, J.A., Schaedler, T.A., Pollock, T.M., 2017. 3D printing of high-strength aluminium alloys. Nature 549, 365–369. doi:10.1038/nature23894

Matweb, 2020. Cr, Fe, Mn, Ni - Material Property Data [WWW Document]. URL http://www.matweb.com (accessed 6.11.20).

Mei, X., Wang, X., Peng, Y., Gu, H., Zhong, G., Yang, S., 2019. Interfacial characterization and mechanical properties of 316L stainless steel/inconel 718 manufactured by selective laser melting. Mater. Sci. Eng. A 758, 185–191. doi:10.1016/j.msea.2019.05.011

Motaman, S.A.H., Roters, F., Haase, C., 2020. Anisotropic polycrystal plasticity due to microstructural heterogeneity: A multi-scale experimental and numerical study on additively manufactured metallic materials. Acta Mater. 185, 340–369. doi:10.1016/j.actamat.2019.12.003

Mumtaz, K.A., Hopkinson, N., 2007. Laser melting functionally graded composition of Waspaloy and Zirconia powders. J. Mater. Sci. 42, 7647–7656. doi:10.1007/s10853-007-1661-3

Neirinck, B., Li, X., Hick, M., 2021. Powder Deposition Systems Used in Powder Bed-Based Multimetal Additive Manufacturing. Accounts Mater. Res. 2, 387–393. doi:10.1021/accountsmr.1c00030

Pragana, J.P.M., Pombinha, P., Duarte, V.R., Rodrigues, T.A., Oliveira, J.P., Bragança, I.M.F., Santos, T.G., Miranda, R.M., Coutinho, L., Silva, C.M.A., 2020. Influence of processing parameters on the density of 316L stainless steel parts manufactured through laser powder bed fusion. Proc. Inst. Mech. Eng. Part B J. Eng. Manuf. 234, 1246–1257.

doi:10.1177/0954405420911768

Repossini, G., Laguzza, V., Grasso, M., Colosimo, B.M., 2017. On the use of spatter signature for in-situ monitoring of Laser Powder Bed Fusion. Addit. Manuf. 16, 35–48. doi:10.1016/j.addma.2017.05.004

Rombouts, M., Kruth, J.P., Froyen, L., Merce, P., 2006. Fundamentals of Selective Laser Melting of alloyed steel powders Fundamentals of Selective Laser Melting of alloyed steel powders. CIRP Ann. - Manuf. Technol. 55, 187–192.

Scaramuccia, M.G., Demir, A.G., Caprio, L., Tassa, O., Previtali, B., 2020. Development of processing strategies for multigraded selective laser melting of Ti6Al4V and IN718. Powder Technol. 367, 376–389. doi:10.1016/j.powtec.2020.04.010

Sing, S.L., An, J., Yeong, W.Y., Wiria, F.E., 2016. Laser and electron-beam powder-bed additive manufacturing of metallic implants: A review on processes, materials and designs. J. Orthop. Res. 34, 369–385. doi:10.1002/jor.23075

Sing, S.L., Lam, L.P., Zhang, D.Q., Liu, Z.H., Chua, C.K., 2015. Materials Characterization Interfacial characterization of SLM parts in multi-material processing : Intermetallic phase formation between AlSi10Mg and C18400 copper alloy. Mater. Charact. 107, 220–227. doi:10.1016/j.matchar.2015.07.007

Suresh, S., 2001. Graded materials for resistance to contact deformation and damage. Science (80-.). 292, 2447–2451. doi:10.1126/science.1059716

Vaezi, M., Chianrabutra, S., Mellor, B., Yang, S., 2013. Multiple material additive manufacturing – Part 1: a review. Virtual Phys. Prototyp. 8, 19–50. doi:10.1080/17452759.2013.778175

Wei, C., Li, L., Zhang, X., Chueh, Y., 2018. 3D printing of multiple metallic materials via modi fi ed selective laser melting. CIRP Ann. - Manuf. Technol. 67, 245–248. doi:10.1016/j.cirp.2018.04.096

Wei, Y., Li, Y., Zhu, L., Liu, Y., Lei, X., Wang, G., Wu, Y., Mi, Z., Liu, J., Wang, H., Gao, H., 2014. Evading the strength-ductility trade-off dilemma in steel through gradient hierarchical nanotwins. Nat. Commun. 5. doi:10.1038/ncomms4580

Yan, J., Ma, J., Wang, J., Shen, Y., 2018. Strength and Ductility with Dual Grain-Size and Texture Gradients in AZ31 Mg Alloy. Metall. Mater. Trans. A Phys. Metall. Mater. Sci. 49, 5333–5338. doi:10.1007/s11661-018-4874-y

Yan, W., Lin, S., Kafka, O.L., Yu, C., Liu, Z., Lian, Y., Wolff, S., Cao, J., Wagner, G.J., Liu, W.K., 2018. Modeling process-structure-property relationships for additive manufacturing. Front. Mech. Eng. 13, 482–492. doi:10.1007/s11465-018-0505-y

Yu, H.Z., Cross, S.R., Schuh, C.A., 2017. Mesostructure optimization in multi-material additive manufacturing: a theoretical perspective. J. Mater. Sci. 52, 4288–4298. doi:10.1007/s10853-017-0753-y

Zavala-Arredondo, M., Ali, H., Groom, K.M., Mumtaz, K., 2018. Investigating the melt pool properties and thermal effects of multi-laser diode area melting. Int. J. Adv. Manuf. Technol. 97, 1383–1396. doi:10.1007/s00170-018-2038-2

List of figures

List of tables